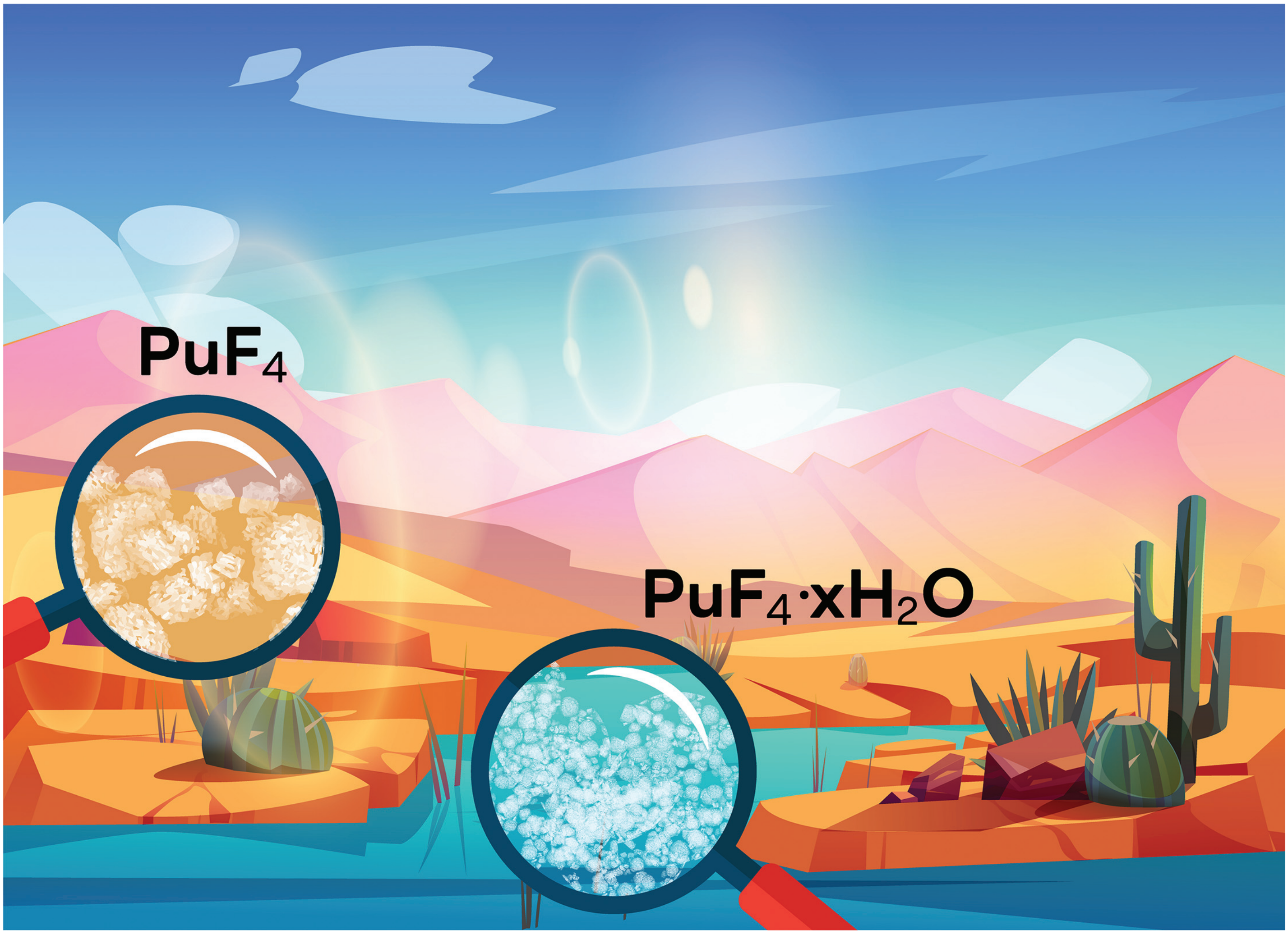

Showcasing research from Eliel Villa-Aleman *et al.*, Savannah River National Laboratory, Aiken, South Carolina, United States.

Chemical and spectroscopic characterization of plutonium tetrafluoride

Anhydrous plutonium tetrafluoride is an important intermediate in the production of metallic Pu. This historically important compound is also known to exist in at least two forms, $PuF_4 \cdot xH_2O(s)$ ($0.5 \le x \le 2$) and $PuF_4 \cdot 2.5H_2O(s)$. We measured the visible and shortwave infrared (SWIR) diffuse reflectance, FTIR, fluorescence, and Raman spectra of $PuF_4(s)$ and $PuF_4 \cdot xH_2O(s)$ to better characterize the material. Our work provides clear indication of the polymeric structure of anhydrous PuF_4, consistent with the Raman spectrum of $UF_4(s)$ and its hydrates.

As featured in:

See Eliel Villa-Aleman *et al.*, *Dalton Trans.*, 2024, **53**, 19166.

ROYAL SOCIETY OF CHEMISTRY

rsc.li/dalton

Registered charity number: 207890

Dalton Transactions

ROYAL SOCIETY OF CHEMISTRY

PAPER

View Article Online
View Journal | View Issue

Cite this: *Dalton Trans.*, 2024, **53**, 19166

Chemical and spectroscopic characterization of plutonium tetrafluoride

Jared S. Kinyon,[a] Eliel Villa-Aleman,*[a] Elodia Ciprian,[b] Amy E. Hixon,[b] Bryan J. Foley,[a] Jonathan H. Christian,[a] Jason R. Darvin,[a] Don D. Dick,[a] Amanda J. Casella,[c] Lucas E. Sweet,[c] Edgar C. Buck,[c] Forrest D. Heller,[c] Aaron D. Nicholas,[c] Cody A. Nizinski[c] and Richard A. Clark[c]

Received 3rd September 2024,
Accepted 16th October 2024

DOI: 10.1039/d4dt02509a

rsc.li/dalton

Anhydrous plutonium tetrafluoride is an important intermediate in the production of metallic Pu. This historically important compound is also known to exist in at least two distinct, yet understudied hydrate forms, $PuF_4{\cdot}xH_2O(s)$ ($0.5 \le x \le 2$) and $PuF_4{\cdot}2.5H_2O(s)$. X-ray diffraction (XRD), thermogravimetric analysis (TGA), and scanning electron microscopy (SEM) are the most common tools used to characterize these materials, often in a context for studying structural and morphological changes that arise from aging or calcination. However, fundamental electronic and vibrational spectroscopic information is rather scarce. Here, we measured the visible and shortwave infrared (SWIR) diffuse reflectance, Fourier transform infrared (FTIR), fluorescence and Raman spectra of $PuF_4(s)$ and $PuF_4{\cdot}xH_2O(s)$ to obtain a better electronic and vibrational fingerprint. Our work provides clear indication of the polymeric structure of anhydrous PuF_4, consistent with the Raman spectrum of $UF_4(s)$ and its hydrates. This is supplemented with XRD, TGA and SEM analysis. Findings in this study indicate that the spectra are modified by particle size, which in turn is influenced by synthetic technique.

Introduction

Since its discovery in 1940, plutonium (Pu) has held a unique position among the chemical elements. Though its destructive capabilities in nuclear weapons will live in infamy, plutonium and the chemical compounds that it forms are of fundamental importance for understanding the chemistry of the actinide series of elements. Despite this, chemical research on plutonium is relatively scarce compared to lighter actinides like uranium and thorium. This scarcity is largely due to a focus on the weaponization of Pu and is exacerbated by the health hazards and proliferation risks that are involved with handling and storing it.

In the early days of plutonium research – not long after Pu was discovered – most studies were application-centric, with a clear focus on maximizing production of Pu metal to develop nuclear arsenals. During this process, plutonium tetrafluoride ($PuF_4(s)$) was discovered to be one of the first plutonium-containing compounds to have utility, leading to its original development during World War II as an intermediate for Pu metal production. Most early studies of anhydrous PuF_4 were metallurgical in nature and focused on optimizing fluorination conditions[1] and engineering better metal recovery,[2,3] with a clear aim to optimize production of Pu metal on an industrial scale.[1–6] This narrow focus of weaponizing Pu provided few opportunities to study the fundamental properties of Pu and its chemical compounds. However, this changed after the collapse of the Soviet Union in 1991, which shifted Pu-based research away from weaponization and towards nuclear waste management and nonproliferation.

To date, the preponderance of Pu-based chemical research has focused on $PuO_2(s)$ due its prevalence in nuclear fuels[7–12] and waste storage.[13] By comparison, there is a dearth of modern studies pertaining to PuF_4.[14–22] This data gap is worsened by the structural instability of PuF_4 and its hydrates. Many stockpiles of anhydrous PuF_4 have degraded and become amorphous due to radiolytic decay, and most research facilities are no longer equipped to produce it, which is typically prepared by high temperature fluorination with highly corrosive HF gas.[18] However, such work is important to understand periodic trends and improve modelling of actinide chemistry. As a general rule, periodic trends for actinide elements are difficult to establish theoretically, which is why experimental techniques such as Raman, infrared (IR), diffuse reflectance, nuclear magnetic resonance (NMR), electron paramagnetic resonance (EPR) and X-ray photoelectron spectroscopies (XPS) are quite useful. Practically, their non-destructive

---

[a] *Savannah River National Laboratory, Aiken, SC, 29808, USA. E-mail: Eliel.villa-aleman@srnl.doe.gov*
[b] *University of Notre Dame, Notre Dame, IN, 46556, USA*
[c] *Pacific Northwest National Laboratory, P.O. Box 999, Richland, WA 99352, USA*

nature has made them well-suited for characterizing materials of importance to the nuclear fuel cycle, such as UF_4 and its hydrates,[23–31] PuO_2 [14,32–41] and various forms of plutonium oxalate.[14,37–40,42] Without foundational experimental data, computational studies of Pu can be quite cumbersome.[43–49]

In this manuscript, we utilize vibrational spectroscopy, X-ray diffraction, microscopy, and thermogravimetric analysis to provide an exquisite look at the structure and morphology of PuF_4 and $PuF_4{\cdot}xH_2O$, thus filling a longstanding knowledge gap, elucidating important trends in the actinide series of elements, and providing new data to improve the accuracy of actinide computational models.

Results and discussion

Structure and morphology

The diffraction pattern of anhydrous PuF_4 (Fig. 1) is consistent with previous studies of PuF_4 [18,19] and isostructural to the anhydrous actinide fluorides NpF_4 and UF_4,[16,50–52] both of which belong to the $C2/c$ space group. Our pXRD data were initially fit to an NpF_4 model[53] and the unit cell parameters were refined to adjust for the slightly smaller Pu atoms. Refined unit cell parameters are not reported due to the uneven surface from our sample preparation. Our analysis resulted in a cell volume that was 14.82 $Å^3$ smaller than NpF_4, which is not unreasonable given that Pu^{4+} is smaller than Np^{4+}.[54] A broad feature around 15° 2θ was consistently measured in our PuF_4 diffractograms but did not fit with our chosen structural model. This feature was not present in the diffraction pattern of the polyimide film that encased our sample. However, as our FTIR results show, this material is hygroscopic, which could explain the presence of this feature.

In contrast, hydrated PuF_4 is known to exist in at least two structurally distinct forms isostructural to the uranium variants—the simple cubic ($Fm\bar{3}m$) and orthorhombic ($Pnma$) geometries for $PuF_4{\cdot}xH_2O$ ($0.5 \leq x \leq 2$) and $PuF_4{\cdot}2.5H_2O$, respectively.[55–57] The 2.5 hydrate is generally stable at room temperature, but infrared measurements have shown that weakly bound water molecules are likely responsible for the variability of x in the cubic form.[26] As shown in Fig. 2, our experimental diffractogram aligns with the published pattern reported by Dawson *et al.* (ICDD #00-034-0515) for the $PuF_4{\cdot}xH_2O$ structure.[55] From a chemical perspective, the relatively simple diffractogram seems rather curious, as $UF_4{\cdot}0.33H_2O$,[27] $UF_4{\cdot}1.33H_2O$[58] and $UF_4{\cdot}2.5H_2O$[31,59,60] are all known to produce numerous diffraction bands that result from a complex structure.

To supplement these results, SEM measurements were conducted on both hydrated and anhydrous PuF_4. Micrographs of $PuF_4{\cdot}xH_2O$ (Fig. 3) reveal that our material contained agglomerates of rounded submicron particles, though the limited resolution hindered a quantitative description of size. The aggregated morphology indicates rapid precipitation from solution, which is supported by earlier solubility experiments.[61] This was experimentally observed when our emerald-green $Pu(NO_3)_4$ solution promptly turned light pink upon the addition of concentrated HF. Synthetic efforts, including cooling reagents, reducing HF concentration, and reducing the rate at which HF was added to $Pu(NO_3)_4$, were attempted to reduce the rate of $PuF_4{\cdot}xH_2O$ precipitation and produce larger particles. Unfortunately, these attempts were unsuccessful.

In contrast, anhydrous PuF_4 possessed larger particle sizes ranging from 5–10 μm in diameter. The particle surfaces were rough with pits and layered edges; such features have been observed after the calcination of Pu(IV) oxalate to PuO_2.[38] Elemental analysis of the material showed no evidence of discrete Pu or F rich regions. However, the anhydrous images (Fig. 3) are quite distinct from those reported on an aged powder produced at Los Alamos National Laboratory (LANL), which primarily consisted of crystalline aggregates 5–20 μm in

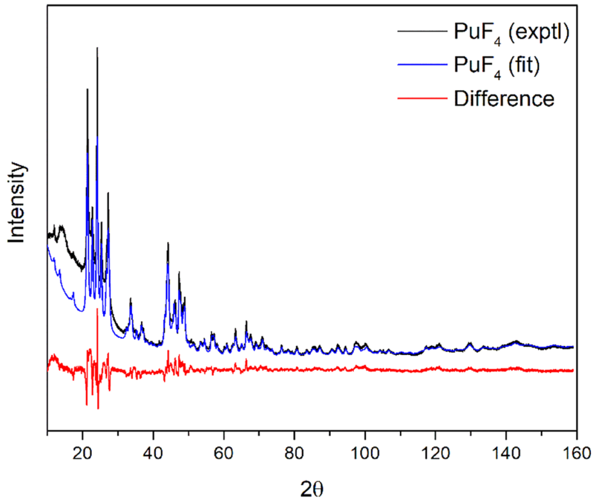

Fig. 1 The observed pXRD pattern of anhydrous PuF_4 (black) is compared to a fit diffraction pattern refined from the known NpF_4 structure (blue), while the difference plot is shown in red.

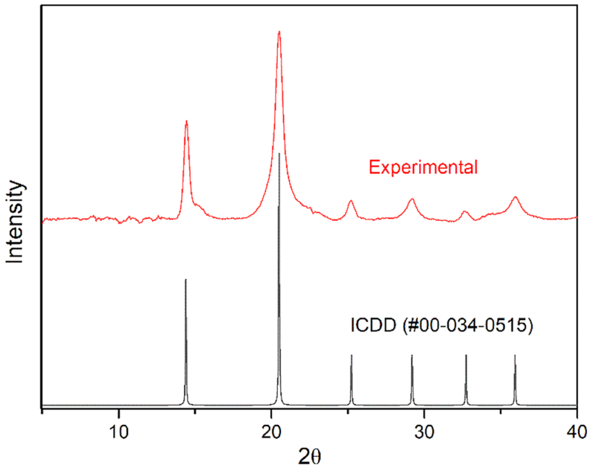

Fig. 2 The experimental and ICDD (#00-034-0515) pXRD patterns of $PuF_4{\cdot}xH_2O$.

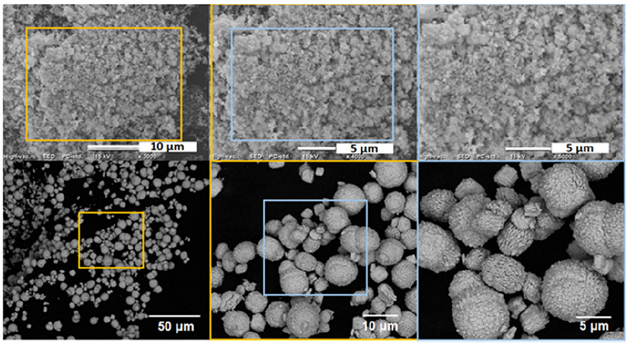

Fig. 3 SEM-SE images of $PuF_4{\cdot}xH_2O$ (top) and SEM-CSE images of anhydrous PuF_4 (bottom) at increasing magnification.

length along their longest dimension.[19] The differing morphologies likely originate from the precipitation and calcination steps, both of which have been shown to affect the size of PuO_2 particulates.[62–65]

TGA was used to measure the mass loss of freshly synthesized $PuF_4{\cdot}xH_2O$ during heating (Fig. 4a). A total weight loss of 6.54 wt% was observed when heated to 800 °C under nitrogen. An initial weight loss of 5.4 wt% occurred from room temperature to 410 °C and is attributed to water removal, which could ostensibly originate from the lattice or surfaced-adsorbed molecules. For a pure lattice contribution, this would correspond with $x = 1$, which is consistent with pXRD results. Additionally, the dehydration is similar to what has been observed for anhydrous PuF_4 with an 8% $PuF_4{\cdot}1.6H_2O$ crystalline phase.[19] The remaining 1.1 wt% loss at 800 °C is assigned to the removal of weakly coordinated fluorine, which has been shown by both Wayne *et al.* and Dawson *et al.* to occur between 300 and 450 °C.[19,55] Another possibility for the remaining mass loss could result from the reaction of PuF_4 and PuO_2 to produce O_2 and PuF_3.[19,66]

The production of both PuF_4 and PuF_3 at high temperatures is further supported by pXRD results of the post-TGA $PuF_4{\cdot}xH_2O$ (Fig. 4b). This is an important observation, as previous literature work on this matter is unclear. For example, under vacuum at 10^{-4} Torr, Dawson *et al.* observed a PuF_3 and PuF_4 mixture when $PuF_4{\cdot}xH_2O$ is heated to 550 °C. For a second sample under vacuum Dawson *et al.* reported PuF_3 and PuO_2 when heating to 900 °C.[56] The same products were produced for a hydrate when heated to 300 °C in an N_2 atmosphere.[55] It was suggested that dehydrated PuF_4 could react with liberated water to produce PuO_2, which in turn reacts with PuF_4 to produce PuF_3. In contrast, Wayne *et al.* did not observe the formation of PuF_3; this is likely due to the use of open crucibles under an Ar atmosphere, which didn't allow for back-reaction with evolved gases.[19] PuO_2 has also been reported as a byproduct of heating $PuF_4{\cdot}xH_2O$ above 300 °C in vacuum or dry nitrogen,[19,55] though its presence can usually be attributed to crystalline impurities inherent to the sample.[18,19] No impurities were found in our sample; however, it is possible undetected impurities reacted with PuF_4.

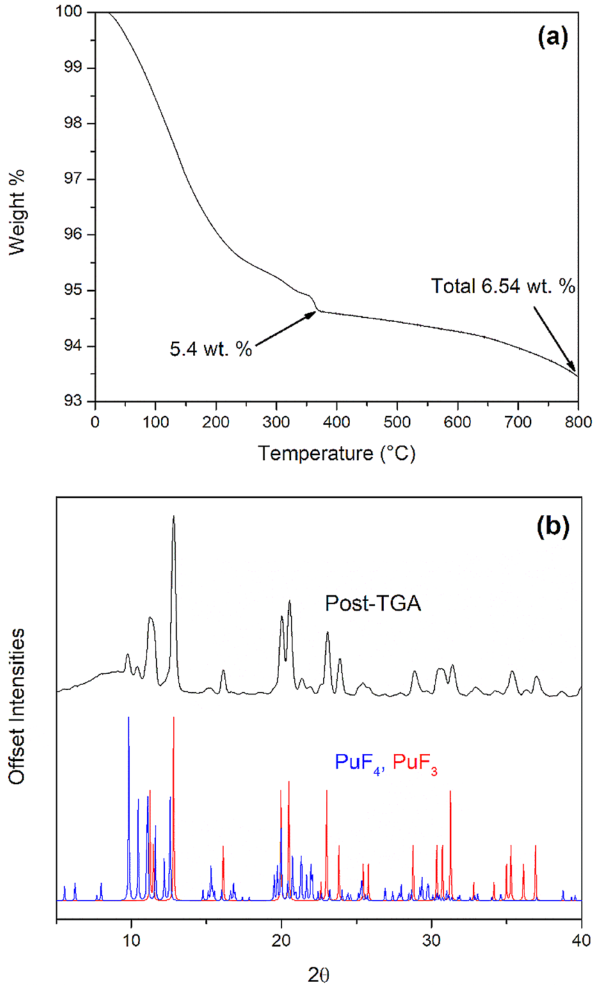

Fig. 4 (a) Thermal decomposition of $PuF_4{\cdot}xH_2O$ under nitrogen heated to 800 °C at a ramp rate of 5 °C min^{-1}. (b) ICDD patterns for PuF_4 (#00-041-1218, blue) and PuF_3 (#00-006-0327, black) in comparison to post-TGA $PuF_4{\cdot}xH_2O$.

Raman spectroscopy

For the first time, Raman spectroscopy was used to elucidate the structures of PuF_4 and $PuF_4{\cdot}xH_2O$. Generally, it is challenging to measure high-quality spectra for metal fluorides because the intensity of Raman bands depend on bond polarizability, and metal–fluorine bonds are weakly polarizable. Fluorescence complicates matters, and has been shown to further obscure signals from $UF_4{\cdot}0.33H_2O$, $U_3F_{12}{\cdot}H_2O$, and $UF_4{\cdot}2.5H_2O$.[24,27,31] We worked under the assumption that both PuF_4 and its hydrate possess a complex polymeric structure, similar to UF_4 and $UF_4{\cdot}2.5H_2O$.[50,59,67]

The Raman spectrum of $PuF_4{\cdot}xH_2O$ (Fig. 5a) primarily features a broad band centered around 400 cm^{-1} and several low intensity bands. The broad feature around 400 cm^{-1} likely results from the small particle morphology of $PuF_4{\cdot}xH_2O$, as Raman spectra can be affected by phonon confinement[68] leading to broad, asymmetric band shapes. Thus, our Raman measurements corroborate the SEM findings.

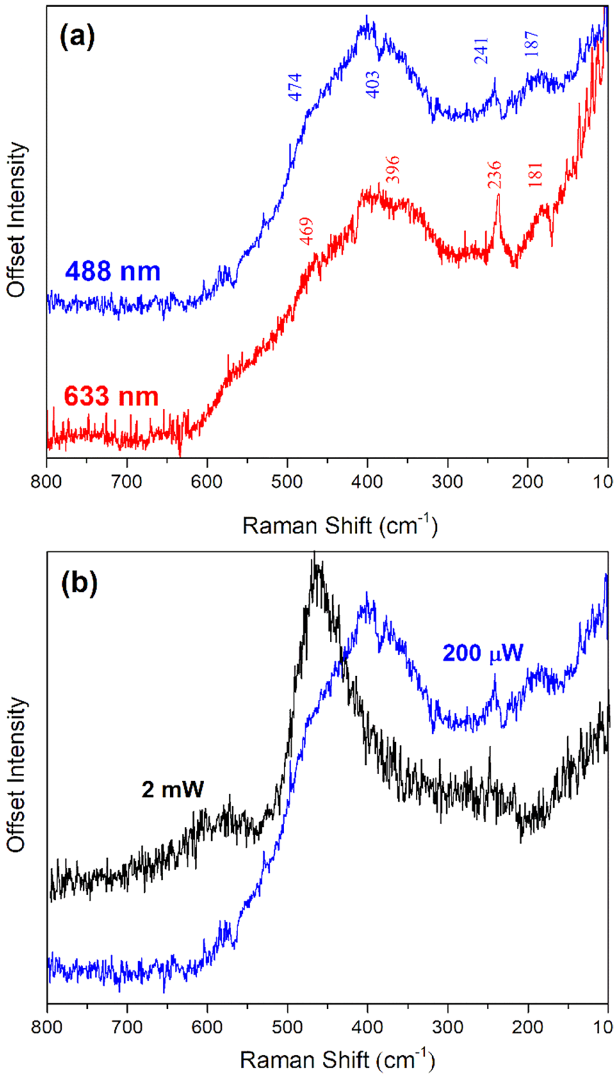

Fig. 5 (a) Raman spectra of $PuF_4{\cdot}xH_2O$ measured at 488 nm (blue) and 633 nm (red). (b) The 488 nm spectrum (blue) measured at 200 µW compared to another measured at 2 mW (black). Both plots are given a dual *y*-axis (intensities) for the convenient comparison of spectral features.

Two challenges were encountered when measuring the Raman spectrum of $PuF_4{\cdot}xH_2O$. First, naturally weak Raman scattering could not be enhanced by increasing laser power since the material was susceptible to decomposition and oxidation upon heating, even with long-term exposure to a low-powered laser. This is unsurprising, as submicron particles are known to undergo laser heating at powers as low as 1 mW. This phenomenon is show in Fig. 5b. At 2 mW, our samples of $PuF_4{\cdot}xH_2O$ had thermally decomposed to PuO_2 nanoparticles, as evidenced by the observation of a broad (FWHM = 20 cm^{-1}) band centered at 465 cm^{-1}, with a weaker shoulder centered near 600 cm^{-1}. Typically, PuO_2 calcined at 450 °C displays a relatively sharp band at 476 cm^{-1} and a broad, weak band at 580 cm^{-1} which correspond to the T_{2g} (1LO1) and 1LO2 bands of PuO_2, respectively.[32–35,69,70] In this case, the FWHM broadening and shift to lower frequencies can be explained by phonon confinement effects and crystallite dimensions of less than 10 nm. Consequently, very low laser powers (<250 µW) and long acquisition times were employed to avoid conversion of both PuF_4 and $PuF_4{\cdot}xH_2O$ to PuO_2.

The second challenge with measuring the Raman spectrum of $PuF_4{\cdot}xH_2O$ is wavelength-dependent fluorescence, which obscures vibrational modes. To determine which spectral features were Raman bands and which were fluorescence, the Raman spectrum of $PuF_4{\cdot}xH_2O$ was measured at 457, 488, 514, and 633 nm laser excitation wavelengths. Spectral features that were reproducible at different excitation wavelengths were labeled and assigned as Raman bands in Fig. 5a, while those shifted in position with respect to excitation wavelength were ascribed to fluorescence (Fig. 6a). Raman bands for $PuF_4{\cdot}xH_2O$ were located near 187, 240, 403 and 474 cm^{-1}, which are in the same spectral region as UF_4 metal–fluorine bands (70 cm^{-1} to 650 cm^{-1}). These low intensity peaks were superimposed on a

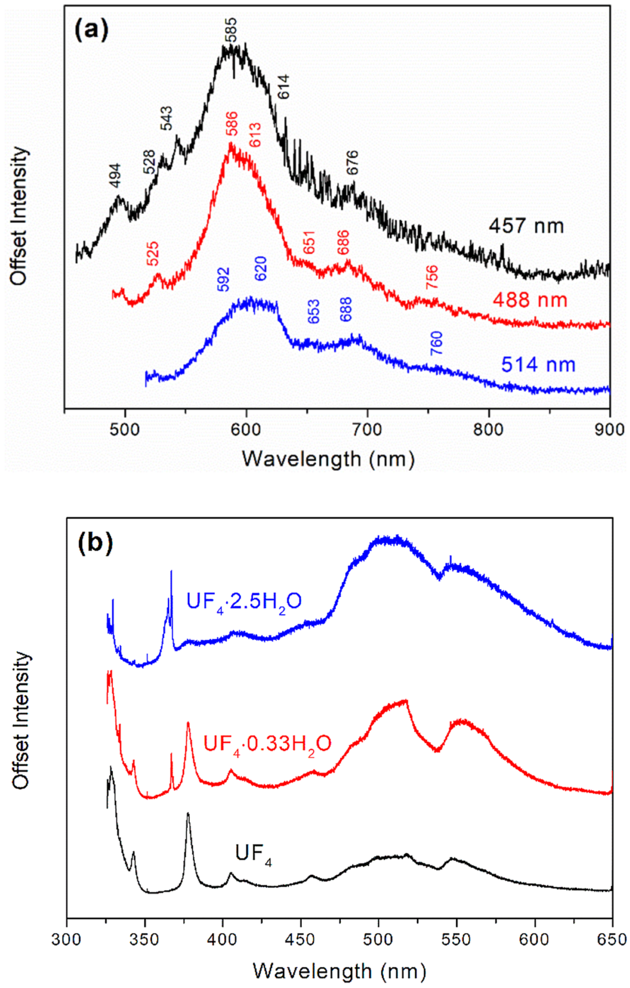

Fig. 6 (a) Fluorescence spectra of $PuF_4{\cdot}xH_2O$ measured with 457 (black), 488 (red), and 514 (blue) nm excitation wavelengths, with respective powers of 444, 172 and 172 µW. (b) Unpublished fluorescence spectra of UF_4 (black), $UF_4{\cdot}0.33H_2O$ (red) and $UF_4{\cdot}2.5H_2O$ (blue) taken at 325 nm.

baseline rising towards the laser excitation wavelength; it is likely that this effect arises ostensibly not from fluorescence, but the significant number of low-frequency modes originating from F–F polymeric interactions and hydrogen bonding from water. Such observations have been made for UF_4 and $UF_4{\cdot}2.5H_2O$.[24,31]

Fig. 6a and Table 1 show the fluorescence spectrum and peak positions, respectively, for $PuF_4{\cdot}xH_2O$ at 457, 488, and 514 nm. The large number of fluorescent features is quite interesting as fluorescent signatures are often used to rapidly assess chemical composition in nuclear forensics, such as for UF_4 particulates.[24,71] Fluorescence spectra collected at different wavelengths possessed a common peak and weak shoulder centered near 600 and 685 nm, respectively. The independence of overall band structure with excitation wavelength indicates that these peaks result from electronic transitions, as would be expected from the Vavilov rule. Larger energy transitions, observed at 457 and 488 nm, may have originated from otherwise inaccessible vibronic states.

Fluorescence generally indicates a preferred relaxation path for excited energy levels. As shown in Fig. 6b, UF_4 and its hydrates have many identical features. This strongly suggests that the origin of the signal is based on the electronic states of U(IV), remaining largely uncoupled from its molecular structure. By analogy, we hypothesize that the fluorescence observed for $PuF_4{\cdot}xH_2O$ arises from different electronic transitions of Pu(IV). The relative strength of the fluorescence bands relative to the Raman could help in the detection and analysis of $PuF_4{\cdot}xH_2O$.

The Raman spectrum of anhydrous PuF_4 (Fig. 7) was markedly different than $PuF_4{\cdot}xH_2O$ and allowed for a more direct comparison with previously published spectra for UF_4. As shown in Fig. 3, anhydrous PuF_4 particles were much larger than $PuF_4{\cdot}xH_2O$, which prevented phonon confinement and spectral broadening. Further, the larger particles of PuF_4 were less susceptible to laser-induced heating during Raman measurements, enabling spectral acquisition using a laser power of to 500 μW, as opposed to 250 μW for $PuF_4{\cdot}xH_2O$. However, long term exposure to laser power still results in the formation of PuO_2, as it does for the hydrate. This work has identified at least 15 Raman bands between 50 cm^{-1} and 400 cm^{-1} and are listed in Table 2. As shown in Fig. 7b, the spectra of PuF_4 and UF_4 share many similarities. The numerous bands in the low frequency region are typical for a fluorine polymeric structure dominating a Raman spectrum[24,27,28,31] and cannot be modeled on the basis of a tetrahedral monomer surrounding Pu.[67]

Table 1 Fluorescent bands (nm) observed for $PuF_4{\cdot}xH_2O$ as a function of laser excitation wavelength (nm)

Fluorescent spectral bands			
Excitation	457	488	514
Bands	494		
	528	525	
	543		
	585	586	592
	614	613	620
		651	653
	676	686	688
		756	760

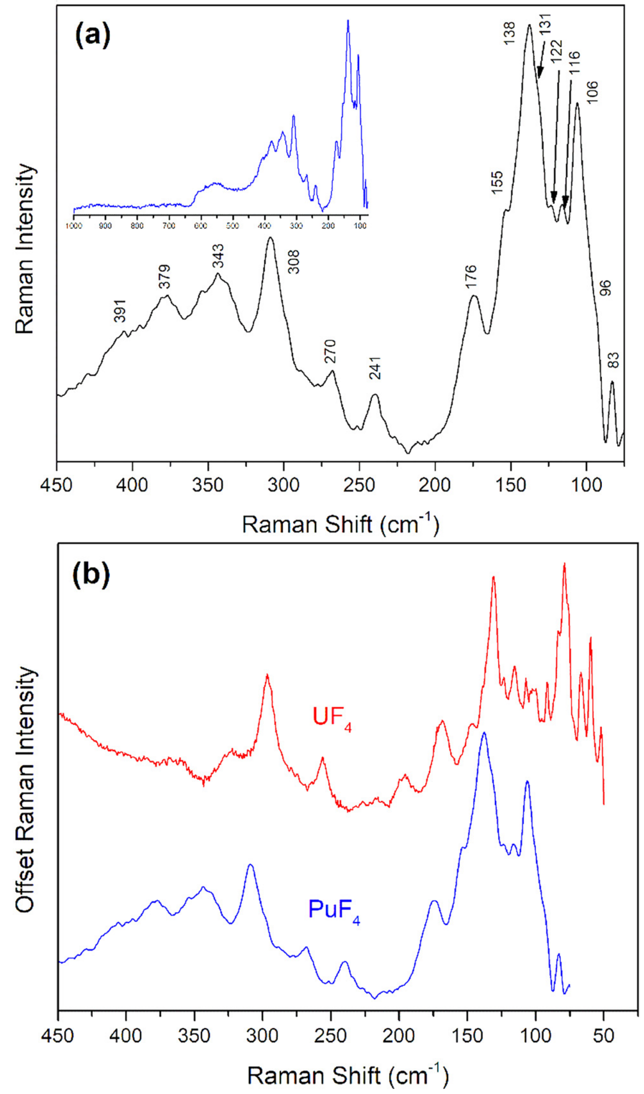

Fig. 7 (a) Raman spectrum of anhydrous PuF_4 measured with an excitation wavelength of 514 nm with bands labeled in the region of interest. The blue inset displays the full spectral range from 50–1000 cm^{-1}. (b) A comparison of the anhydrous variants of UF_4 (red)[24] and PuF_4 (blue) Raman spectra taken at 514 nm. Plot is given a dual y-axis for convenient comparison of spectral features.

Infrared spectroscopy

FTIR was used to gain a more complete picture of the vibrational modes of the water molecules absorbed in PuF_4 and $PuF_4{\cdot}xH_2O$ and are shown in Fig. 8, while the peak positions are listed in Table 3. These measurements are interesting since most infrared measurements on solid-state Pu(IV) samples are limited,[38,42,72,73] with most of literature focusing

Table 2 Raman spectral bands for PuF_4 and $PuF_4 \cdot xH_2O$, as labeled in Fig. 5, are compared to bands previously measured for UF_4[24] and $UF_4 \cdot 0.33H_2O$.[27] Save for the cubic $PuF_4 \cdot xH_2O$, the crystallographic structures are all similar and belong to *C*2/*c*

Raman spectral bands			
UF_4	PuF_4	$UF_4 \cdot 0.33H_2O$	$PuF_4 \cdot xH_2O$
		50.9	
59.4			
66.8		61.7	
78.9	82.7	76.6	
		84.8	
91	96.3		
		93.3	
		96.8	
101.3		102	
107.2	105.8	108	
115.9	116.2	118	
	122.5	125	
131.4	130.6	132	
	138.1	141	
148.5			
	155.1		
170.4	175.6	175	
			187
197.3			
			236
	240.7		241
255.8			
	270.2		
296.1			
	307.7	307	
322.4			
		332	
	342.5		
360.8		363	
	378.5	382	
	391		
			403
			474
603.6			
		637	
		3532	
		3602	

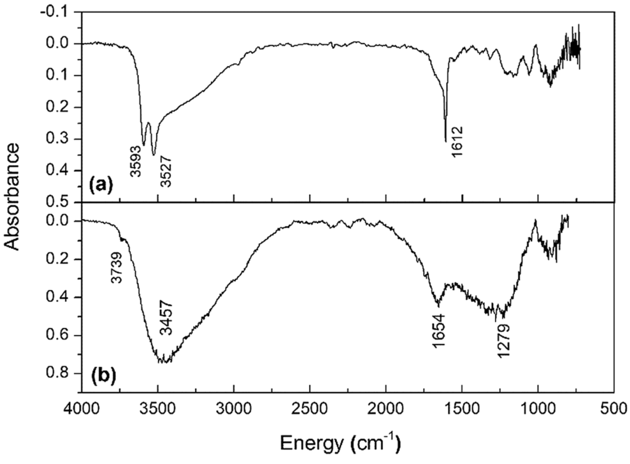

Fig. 8 Room-temperature FTIR spectra of (a) anhydrous PuF_4 and (b) $PuF_4 \cdot xH_2O$ taken at room temperature.

on the analysis of aqueous solutions in the presence of species such as ClO_4^-, Cl^-, NO_3^- and HNO_3.[74]

Generally, actinide–fluoride bonds are not expected to possess IR active modes at frequencies greater than 500 cm^{-1}. This is best reflected by the FTIR spectrum of anhydrous UF_4, which has been shown to have no active vibrational mode between 500–4000 cm^{-1}.[31] This result is supported by DFT calculations, which predicted no IR-active modes for UF_4 above 400 cm^{-1}.[23] Therefore, it is expected that the peaks for $PuF_4 \cdot xH_2O$ and PuF_4 displayed in Fig. 8 are related to water, OH stretches and low-frequency modes. The water band features in the anhydrous spectrum suggests either the presence of natural impurities (*e.g.*, a small contribution of $PuF_4 \cdot xH_2O$ within the anhydrous lattice) or an active sorption process, presumably from adsorbed water molecules or an isostructural hydrate with $x < 0.5$.

The sharp bands at 3593 cm^{-1} and 3527 cm^{-1} observed in the anhydrous spectrum of PuF_4 (Fig. 8a) are superimposed on a broad band indicative of free OH experiencing different chemical environments within the crystal lattice,[31] while the broad band itself suggests the presence of hydrogen bonding and polymeric fluorine bonding modes. The long tail from hydrogen/fluorine bonding has been observed in IR spectra of UO_2F_2-$(H_2O)_x(HF)_y$[75–78] and water with significant HF interactions.[79] The asymmetry of the OH region likely results from broad, overlapping hydrogen-bonded OH peaks in slightly different chemical environments.[31] Similar spectral features have been observed for $UF_4 \cdot 0.33H_2O$[27] and $UF_4 \cdot 2.5H_2O$.[31] Multiple peaks likely arise from OH groups weakly interacting with oxygen or fluorine neighbors.

At 1612 cm^{-1}, there is another sharp peak overlayed on a weak asymmetric feature. The sharp band suggests an HOH bending mode in a specific configuration, while the weak broader asymmetrical component could be evidence of HOH bending in multiple chemical environments. A comparison to IR data from Khanaev *et al.*[26] suggests that $PuF_4 \cdot 0.33H_2O$ may have been the hydrate in the sample prepared at PNNL and analyzed at SRNL. Though the means of H_2O introduction to the sample remains unknown, it can be noted that PuF_4 was synthesized in the arid environment in which PNNL is located. It is possible that anhydrous PuF_4 absorbed most of the water once exposed to the more humid environment experienced at SRNL. Further research is warranted to examine whether the environment in which PuF_4 is synthesized or handled can answer material provenance questions relevant to nuclear forensics.

The peaks for $PuF_4 \cdot xH_2O$ (Fig. 8b) are related to water molecules in different chemical environments corresponding to OH stretches, H_2O bending modes and low-frequency modes. FTIR data has been described in detail for $PuF_4 \cdot xH_2O$ (x = 2.3, 0.9, 0.6 and 0.3) and closely matches the results from our material.[26] Table 3 compares our results to the x = 2.3 and x = 0.3 variants. The sharp shoulder peak at 3739 cm^{-1} is likely related to a free OH functional group; these usually have limited interactions with fluorine or water due to steric effects, resulting in shaper, higher-frequency bands with a FWHM <

Table 3 FTIR peaks for PuF_4 and its hydrate. A comparison to peaks from the literature for $UF_4{\cdot}0.33H_2O$, $PuF_4{\cdot}2.3H_2O$ and $PuF_4{\cdot}0.3H_2O$ is given for convenience. Experimental peaks are labeled in Fig. 8

	$UF_4{\cdot}0.33H_2O$[27]	$PuF_4{\cdot}2.3H_2O$[26]	$PuF_4{\cdot}0.3H_2O$[26]	$PuF_4{\cdot}xH_2O$	PuF_4
O–H	3589			3739	3595
	3518	3525			3527
	3431	3375	3280	3457	
	3237	3200			
H_2O			1725		
			1705		
	1608	1650		1654	1612
	1556	1629	1632		
?				1279	
O–H*			789		
			769		
H_2O/F	427	650			
		560	560		
		480	490		
		440	445		
An-F	400	400	400		

50 cm^{-1} when compared with more strongly interacting OH groups. This contrasts with the broad, lower frequency peak at 3457 cm^{-1} seen in $PuF_4{\cdot}xH_2O$, which is much more typical for a hydrogen-bonded OH group.[27] Finally, an HOH bending mode common for hydrated lattices can be observed at 1654 cm^{-1}.[26,27] Comparisons with the UF_4 hydrates strongly suggest that the water/PuF_4 ratios are higher for $PuF_4{\cdot}xH_2O$ than for $UF_4{\cdot}2.5H_2O$.[31] Though this would contradict the TGA results, the hydrated PuF_4 structure is based on submicron particulates and likely affected by surface properties. Considering this, it is very likely that this sample could have sorbed water between measurements.

Diffuse reflectance spectroscopy

Diffuse reflectance spectroscopy (DRS) is a useful tool for analyzing the local electronic structure of actinides, including plutonium tetrafluoride. While both Raman and infrared spectroscopy help elucidate local site symmetry, DRS is advantageous because of its sensitivity to *electronic* metal–ligand interactions. This allows it to provide detailed information based on the splitting of Laporte-forbidden f–f transitions due to the influence of the crystal field,[14,15,80–82] making it highly sensitive to changes in the lattice symmetry resulting from alterations to oxidation state or structure.[83] Its immunity to fluorescence, which often stymies the acquisition of Raman spectra, makes it an attractive technique.

The room-temperature DRS spectra for both PuF_4 and $PuF_4{\cdot}xH_2O$ are displayed in Fig. 9. These measurements are significant, as the available modern literature for diffuse reflectance on solid-state Pu complexes is limited, focusing instead on Pu-based coordination complexes arising from aqueous solvents,[84–86] organic solvents,[87–92] ionic liquids[93] and solid-state melts.[94] In the solid state, the primary interest in DRS has been to investigate the solubility and oxidative stability of Pu(IV) in solid matrices to assess their suitability for waste storage.[95–98] Only recently have the oxalates and oxides been scrutinized with modern instrumentation.[37,86]

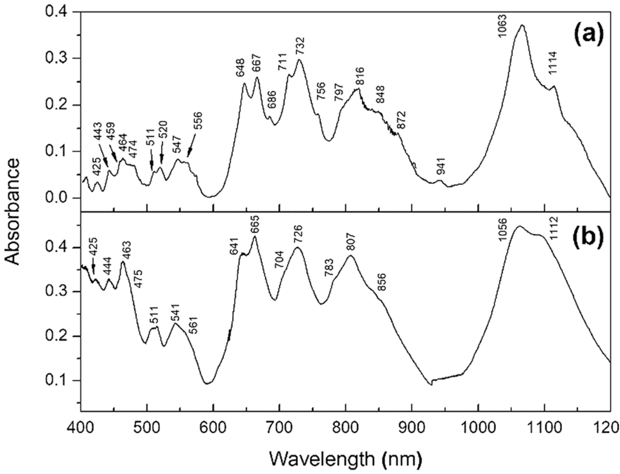

Fig. 9 DRS spectra in the visible and shortwave infrared (SWIR) of (a) PuF_4 and (b) $PuF_4{\cdot}xH_2O$ taken at room temperature.

Each spectrum features a complex combination of several relatively broad and sharp features from 400–1200 nm. Despite their known differences in crystallographic symmetry, many of the spectral features and positions of $PuF_4{\cdot}xH_2O$ were shared with anhydrous PuF_4, with the primary difference being in the broadness of the peaks, especially below 600 nm. The presence of water in the hydrate allows for greater overlap between the electronic bands resulting in peak broadening. The broadening of peaks observed in the hydrate could also be reflective of our SEM and XRD results; given that it is more amorphous than PuF_4, and that DRS is sensitive to the degree of crystallinity, the DRS spectrum of the hydrate should be expected to possess broader peaks than the anhydrous variant. The relative intensity increases for the hydrate peaks, such as at 464 and 1114 nm are not currently understood, but could be explained by changes in the local symmetry, since the crystal-field plays an important role in transition probability.

Though not exhaustive, the DRS peaks are listed in Table 4 and compared to literature values. This includes the room-temperature DRS spectrum of plutonium tetrafluoride measured by Hobart *et al.* for a presumably anhydrous sample from 400–700 nm (ref. 14) and is shown in the inset of Fig. 10. The spectral features in the measured range match well, indicating no changes to the oxidation state of Pu(IV). The offset in peak position could be attributed to calibration issues. Given that the peak positions/intensities best match anhydrous PuF_4 rather than $PuF_4{\cdot}xH_2O$, our work clarifies that the original measurement was likely performed on an anhydrous sample. We also identified an additional peak at 686 nm and extended the range of the original measurement.

Also worth mentioning is the experimental work of Carnall *et al.*[15] measured the absorbance spectrum of anhydrous PuF_4 pressed into a KBr pellet at 4 K from 360–2500 nm. Although band intensities might somewhat differ between absorbance and diffuse reflectance spectra, both provide the same information with regard to peak position and serves as a useful point of reference for the interpretation of our experimental results. Additionally, the low temperature of the measurement reduced spectral crowding and allowed for the identification of ground-state transitions. As seen in Fig. 10, there is good agreement in the absorption spectrum and our DRS results; peaks with similar central positions are listed in Table 4. Lower temperature measurements would be expected to cause further sharpening and splitting of the room temperature peaks.

Table 4 Experimentally-determined DRS peak positions for anhydrous PuF_4 and $PuF_4{\cdot}xH_2O$. For convenience, these are compared to previously measured values for plutonium tetrafluoride, with italic values being estimates based on the provided literature plots in Fig. 10. The degree of hydration for literature samples is unclear, and many of the sharper splittings visible only at low temperatures are not included for brevity

PuF_4 [14]	PuF_4 [15]	PuF_4	$PuF_4{\cdot}xH_2O$
421	*426*		425
440		443	444
	459		
460	*464*	464	463
470	*473*	474	475
506	*509*	511	511
513	*519*	520	
540	*534*	547	541
551	*562*	556	561
	572	574	
638	*645*	648	641
656	*663*	667	665
		686	
	710	711	704
	724	732	726
	753	756	
	788	797	783
	808	816	807
	826		
	842	848	856
	860		
	873	872	
	921	941	
	1060	1063	1056
	1093		
		1114	1112
	1170		

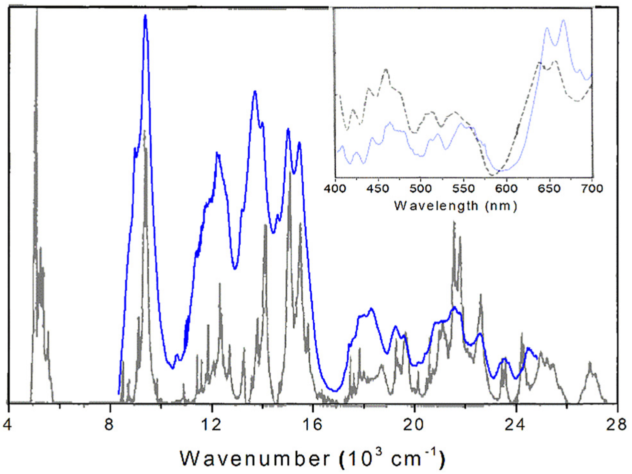

Fig. 10 DRS spectra of anhydrous PuF_4 at room temperature (blue), compared with its absorbance measured at 4 K (black, reproduced from ref. 15 with the permission of AIP Publishing). The inset depicts another comparison of our PuF_4 DRS spectrum to an earlier one made at room temperature.[14]

Conclusions

The crystallinity, morphology and optical properties of anhydrous PuF_4 and one of its hydrates, $PuF_4{\cdot}xH_2O$, were studied with a variety of spectroscopic and microscopic techniques. Initial pXRD results showed a few peaks for $PuF_4{\cdot}xH_2O$, as opposed to the more complex diffractogram expected for anhydrous PuF_4 or the other hydrate, $PuF_4{\cdot}2.5H_2O$. These results were augmented by SEM, which provided a clear difference in particulate dimensions prepared from the dry and wet methods. In particular, the wet method showed preferential submicron particulate formation of $PuF_4{\cdot}xH_2O$ resulting from rapid precipitation, in stark contrast to the large PuF_4 agglomerates produced *via* dry synthesis. Additionally, TGA and post-XRD measurements clarified that the majority of mass lost from heating $PuF_4{\cdot}xH_2O$ occurs due to dehydration of the hydrate; an assumption of pure bonding and negligible adsorption would lead to an estimate of $x = 1$, which is consistent with pXRD results. The presence of PuF_3 above 800 °C likely arises from the closed, non-oxidizing atmosphere of the TGA.

For the first time, the Raman spectra of both PuF_4 and $PuF_4{\cdot}xH_2O$ were recorded with several wavelengths. In particular, the spectrum of $PuF_4{\cdot}xH_2O$ was found to produce a poor signal, even when compared to UF_4 and its hydrates. In addition to weak polarizability, broad bands and a rising baseline made interpretation quite difficult. A rising baseline likely arises from F–F agglomerates and hydrogen bonding from water, whereas peak broadness can be explained by phonon confinement of the small particulates. In contrast, anhydrous

PuF_4 had a much stronger response with sharper, well-defined Raman bands. Their spectral location closely mirrors UF_4, representing a set of isostructural compounds (UF_4, CeF_4, *etc.*) where F–F vibrational modes dominate the Raman spectrum. The fluorescence spectra of $PuF_4{\cdot}xH_2O$ was also investigated and found to have bands analogous to those observed from UF_4 and its hydrates, suggesting the presence of electronic transitions that could be used to identify PuF_4 and its hydrates.

The water content was found to clearly impact the IR spectrum of both anhydrous PuF_4 and $PuF_4{\cdot}xH_2O$ at higher energies, especially since no metal–fluoride peaks were expected below 500 cm^{-1}. Bands corresponding to water bending or OH stretch modes in dry PuF_4 suggest that water was sorbed during synthesis at PNNL or during handling in the humid environment at SRNL. Finally, DRS in the visible and short-wave infrared for both anhydrous PuF_4 and $PuF_4{\cdot}xH_2O$ closely match earlier literature reports for PuF_4. Save for peak broadening in $PuF_4{\cdot}xH_2O$, the almost matching spectra indicate that excess water does not affect the electronic interactions between fluoride and Pu(IV) ions.

Experimental

Synthesis

All plutonium syntheses were performed inside Hazard Category II nuclear facilities that permit the safe handling of weapons-grade (WG) plutonium (>93% ^{239}Pu). Anhydrous PuF_4 was prepared at Pacific Northwest National Laboratory (PNNL) by first purifying WG Pu(IV) nitrate using anion exchange chromatography. The purified Pu was then precipitated as Pu(IV) oxalate through addition of oxalic acid. The oxalate was then calcined to PuO_2 in air at 300 °C. The resulting PuO_2 was then converted to PuF_4 by reaction with anhydrous HF gas using the experimental set-up described by Casella *et al.*[21] Briefly, PuO_2 was heated to 300 °C in an air/O_2 mixture. The atmosphere was then converted to an HF/O_2 mixture, and the temperature was increased and held at 480 °C for 2 hours. The final product had a light pink color that was consistent with previous descriptions of PuF_4. The product was subsequently analyzed by powder X-ray diffraction (pXRD) to determine purity and reaction yield.

A hydrated sample of PuF_4, henceforth referred to as $PuF_4{\cdot}xH_2O$, was synthesized *via* low-temperature hydrofluorination of WG Pu. Specifically, 8.4 mL of 1 M HF was added to 21.45 mL of 0.098 M $Pu(NO_3)_4(aq)$ to immediately yield a light pink solid that was dried overnight under a flow of argon. To limit the effects of radiolytic decay on chemical structure, all samples were analyzed readily after their production.

Powder X-ray diffraction

PuF_4 was prepared by loading ~1 g of powder into a 3D-printed sample holder with a μm thick polyimide film window. Powder X-ray diffraction data was collected using a Rigaku Ultima IV diffractometer equipped with a Cu sealed tube X-ray source and a 5° linear position sensitive detector on a 285 mm radius goniometer. Cu K-α X-rays were selected by use of a Ni filter. Diffraction data was collected from 5–159° 2θ in intervals of 0.02°. Data was analyzed using TOPAS version 6.[99]

Diffractograms of $PuF_4{\cdot}xH_2O$ were collected with a Bruker Quazar single crystal X-ray diffractometer (SC-XRD) featuring monochromated Mo K-α radiation. The utilization of an SC-XRD as opposed to a powder X-ray diffractometer (pXRD) led to broader diffractograms, a feature primarily attributed to the lower resolution of the SC-XRD detector. The diffractometer had a 1024 × 1024 resolution and was positioned at a distance of 200 mm. Phi scans were conducted over 360° for a duration of up to 720 s, ranging from 4° to 54° 2θ, and diffractograms were obtained by integrating the resulting Debye rings. Diffractograms were obtained for freshly synthesized $PuF_4{\cdot}xH_2O$ both before and after subjection to thermogravimetric analysis (TGA). To address 2θ displacement, we employed lanthanum hexaboride (LaB_6(s); Alfa Aesar, 99.5%) as an external standard. The International Centre for Diffraction Data (ICDD) database of crystal and powder X-ray diffraction[100] was used for phase matching.

TGA

Thermogravimetric analysis (TGA) was used to provide information on $PuF_4{\cdot}xH_2O$ water content and probe chemical changes of hydrated PuF_4 as a function of temperature. $PuF_4{\cdot}xH_2O$ (11.40 mg) was placed inside an alumina crucible and heated to 800 °C at a ramp rate of 5 °C min^{-1} and a sampling interval of 2 s pt^{-1}. A balance flow rate of 50 mL min^{-1} and a sample flow rate of 80 mL min^{-1} was used during sample measurements. Increased flow rates were used to prevent corrosion of the instrument due to release of HF during heating.

SEM

The imaging analysis for anhydrous PuF_4 was performed using a Thermo-Fisher Inc., (Hillsboro, OR) Quattro Field Emission Gun (FEG) scanning electron microscope (SEM) equipped with a circular backscattered electron (CSE) detector and an iXRF Systems (Austin, TX) X-ray energy dispersive spectroscopy (EDS) detector. The system was modified to handle radioactive materials and the vacuum pumping system of the microscope was connected to a series of high efficiency filters to prevent the release of radioactivity to the environment. A beam energy of 20 keV was effective at revealing the light elements (F–K line) and the heavy element Pu–M line efficiently. The spatial resolution of the elemental mapping was unlikely to be better than 1 μm^2.

A JEOL JCM-6000 Plus Neoscope benchtop SEM was used to study the morphology of hydrated plutonium fluoride materials. Images were obtained using accelerating voltages ranging from 10 to 15 kV, with magnification reaching up to 5000× under secondary electron (SE) mode. To mitigate the hazards associated with handling dispersible plutonium, all sample materials were prepared within a negative pressure glovebox, and a minimal amount of plutonium powder was meticulously dispersed on carbon tape affixed to an aluminum stub. These stubs were tested for robustness and dispersibility then loaded out of the glovebox onto the benchtop.

Raman spectroscopy

Plutonium samples were contained within a double-walled containment cell containing BaF_2 transmission windows for all vibrational spectroscopy and diffuse reflectance measurements. Raman and fluorescence spectra were acquired with a LabRAM HR800 (Horiba Jobin–Yvon) μ-Raman spectrometer equipped with an Andor iDus charge coupled device (CCD) detector (DU146A-LDC-DD). The detector had a 15 μm pixel resolution and a 2000 × 256 pixel array, and most experiments were conducted by binning the spectral array by a factor of two. The detector was maintained at a temperature of −92 °C with the aid of a water chiller and thermoelectric cooling. Excitation wavelengths of 457, 488, 514, and 633 nm were used, and spectra were processed using bandpass filters from Semrock Inc. The laser was focused onto the sample with a 50× objective and power at the sample ranged from 100–500 μW. Laser power was controlled by a half-wave plate and polarizer. Specular reflection from the sample was eliminated with ultra-steep, long pass edge filters produced by Semrock Inc., and an 1800 g mm^{-1} grating was used to disperse light onto the detector. Data acquisition periods ranged from 1–12 h. Labspec 5.78 software was used to control data acquisition parameters. For each integration time, at least two additional spectra were co-added to remove cosmic ray contributions. Fluorescence measurements were recorded using a 600 g mm^{-1} grating up to 900 nm with 457, 488, and 514 nm excitation for $PuF_4{\cdot}xH_2O$ samples. Acquisition periods for fluorescence measurements lasted approximately 5 minutes. Additional post-processing, including background subtraction, peak smoothing (10-point adjacent averaging), and peak fitting were conducted in OriginPro; all peaks were assumed to have a Lorentzian line shape.

Infrared spectroscopy

Diffuse reflectance Fourier transform infrared spectroscopy (DRIFTS) was performed with a Continuum IR microscope coupled to a Nicolet 6700 spectrometer. A 15× Reflachromat objective from Thermo Fisher was used to focus light onto samples. A mercury cadmium telluride (MCT) detector, cooled with liquid nitrogen, was used to record the interferograms. Spectra were collected over a 800–7500 cm^{-1} spectral window with 4 cm^{-1} resolution. The BaF_2 windows of the double-walled containment cell limited optical transmission to energies >800 cm^{-1}. A data acquisition period consisted of the average of 2000 individual spectra, and multiple measurements were taken to ensure reproducibility. Baseline correction was performed with OriginPro software.

Diffuse reflectance spectroscopy

An Olympus microscope coupled to an Andor Kymera 328i scanning spectrometer was used to perform diffuse reflectance spectroscopy (DRS) measurements. Illumination was provided with an Olympus quartz tungsten halogen (QTH) lamp with a spectral range of 400–2500 nm. Light was passed through a polarizer and focused onto the sample with an Olympus 20× objective. Reflected light polarized perpendicular to the incident light was collected with the objective at normal incidence, directed to a lens, focused into a broadband fiber optic with low OH content, and then directed into the Kymera 328i spectrometer. Three spectral regions were collected that used two different detectors and three different gratings. The first spectral range, 400–900 nm, was collected with an Andor Newton (DU920P-DU2) CCD detector and a 1200 g mm^{-1} grating blazed at 500 nm. The second spectral range, 600–1200 nm, was collected with and Andor iDus InGaAs-1.7 detector and 600 g mm^{-1} grating blazed at 1000 nm. The third spectral range, 930–1600 nm, was collected with an Andor iDus InGaAs-1.7 detector and a 600 g mm^{-1} grating blazed at 1200 nm. A longpass edge filter (900 nm) was used to block visible light that could result in second order reflections and produce false signals in the InGaAs detector. The spectral resolution was 1.0 nm. The system was calibrated, across the three spectral ranges, with the 404.7, 435.8, 576.96, 579.1, 696.5, 763.5, 811.5, 866.8, 912.3, 965.8, 1047.1, 1148.8, 1211.2, 1295.7, 1331.3, 1529.9 nm lines of a HgAr lamp. Spectralon placed in the double-walled cell was used to collect a reference spectrum, and Andor Solis software was used to collect absorption data. The three regions were then stitched together to construct the spectrum. Manual adjustments to the absorbance were unnecessary.

Author contributions

Jared S. Kinyon: writing – original draft, writing – review and editing, visualization. Eliel Villa-Aleman: writing – original draft, writing – review and editing, data curation, conceptualization. Elodia Ciprian: writing – review and editing, data curation. Amy E. Hixon: writing – review and editing, resources. Bryan J. Foley: writing – review and editing, resources. Jonathan H. Christian: writing – review and editing, funding acquisition, project administration, conceptualization, resources. Jason R. Darvin: writing – review and editing, data curation, investigation. Don D. Dick: writing – review and editing, data curation. Amanda J. Casella: writing – review and editing, resources. Lucas E. Sweet: writing – review and editing, visualization, data curation, formal analysis. Edgar C. Buck: writing – review and editing, data curation, investigation. Forrest D. Heller: writing – review and editing. Aaron D. Nicholas: writing – review and editing. Cody A. Nizinski: writing – review and editing, data curation, investigation. Richard A. Clark: writing – review and editing.

Data availability

Detailed datasets, including raw data and processed results, are available from the corresponding author upon reasonable request.

Conflicts of interest

There are no conflicts to declare.

Acknowledgements

This work was funded by the Office of Defense Nuclear Nonproliferation Research and Development within the U.S. Department of Energy's National Nuclear Security Administration for the synthesis of PuF_4 and material characterization. This work was produced by Battelle Savannah River Alliance, LLC under Contract No. 89303321CEM000080 and/or a predecessor contract with the U.S. Department of Energy. Publisher acknowledges the U.S. Government license to provide public access under the DOE Public Access Plan (**https://energy.gov/downloads/doe-public-access-plan**). The United States Government retains and the publisher, by accepting this article for publication, acknowledges that the United States Government retains a non-exclusive, paid-up, irrevocable, worldwide license to publish or reproduce the published form of this work, or allow others to do so, for United States Government purposes.

References

1 I. B. Johns and G. H. Moulton, *Large-scale Preparation of the Anhydrous Fluorides of Plutonium*. Report LA–193, Los Alamos Scientific Laboratory, Los Alamos, NM, 1944.

2 R. D. Baker, *Preparation of plutonium metal by the bomb method*. Report LA–473, Los Alamos Scientific Laboratory, 1946.

3 W. V. Conner, *Process studies on the reduction of plutonium tetrafluoride to metal*, Rocky Flats Div., Dow Chemical Co., Golden, Colo, 1966.

4 W. S. Moser and J. D. Navratil, Review of major plutonium pyrochemical technology, *J. Less-Common Met.*, 1984, **100**, 171–187.

5 I. B. Johns, *Equilibrium Constants and Heats of Reaction for the Hydrofluorination of Uranium Dioxide and Plutonium Dioxide*, United States, 1945.

6 D. L. Clark, *et al.*, *Plutonium*, Springer, 2006.

7 M. Le Guellec, *et al.*, Grain size analysis and characterization by Raman spectroscopy of a homogeneous sintered MOX fuel, *J. Eur. Ceram. Soc.*, 2022, **42**(16), 7553–7560.

8 Z. Talip, *et al.*, Characterization of un-irradiated MIMAS MOX fuel by Raman spectroscopy and EPMA, *J. Nucl. Mater.*, 2018, **499**, 88–97.

9 C. Jegou, *et al.*, Raman micro-spectroscopy of UOX and MOX spent nuclear fuel characterization and oxidation resistance of the high burn-up structure, *J. Nucl. Mater.*, 2015, **458**, 343–349.

10 C. G. Worley and G. J. Havrilla, Micro-X-ray Fluorescence Characterization of Mixed Oxide Fuel Surrogate Feed Material, *Anal. Chem.*, 1998, **70**(14), 2957–2963.

11 T. Abram and S. Ion, Generation-IV nuclear power: A review of the state of the science, *Energy Policy*, 2008, **36**(12), 4323–4330.

12 Status and Advances in MOX Fuel Technology, series=Technical Reports Series. 2003.

13 L. Tandon, *Radiolysis of Salts and Long-Term Storage Issues for Both Pure and Impure PuO_2 Materials in Plutonium Storage Containers*, United States, 2000.

14 D. E. Hobart, *et al.*, *Formation, characterization, and stability of plutonium(IV) colloid; A progress report*, United States, 1989.

15 W. T. Carnall, *et al.*, Analysis of the crystal–field spectra of the actinide tetrafluorides. I. UF_4, NpF_4, and PuF_4, *J. Chem. Phys.*, 1991, **95**(10), 7194–7203.

16 S. Kern, *et al.*, Temperature variation of the structural parameters in actinide tetrafluorides, *J. Chem. Phys.*, 1994, **101**(11), 9333–9337.

17 C. Capan, *et al.*, Probing the Pu^{4+} magnetic moment in PuF_4 with ^{19}F NMR spectroscopy, *Phys. Rev. B*, 2016, **93**(22), 224409.

18 K. McCoy, *et al.*, Radiation damage and annealing in plutonium tetrafluoride, *J. Nucl. Mater.*, 2017, **496**, 379–387.

19 D. M. Wayne, *et al.*, X–ray diffraction, differential scanning calorimetry and evolved gas analysis of aged plutonium tetrafluoride (PuF_4), *J. Radioanal. Nucl. Chem.*, 2021, **329**(2), 741–756.

20 E. D. Walter, *et al.*, Measurement of local magnetic fields in actinide tetrafluorides, *J. Chem. Phys.*, 2021, **154**(21), 211101.

21 A. J. Casella, *et al.*, In Stream Monitoring of Off-Gasses from Plutonium Fluorination, *Actinide Res. Quart.*, 2019, (Second Quarter), 31–35.

22 L. E. Cox and J. D. Farr, 4f binding-energy shifts of the light-actinide dioxides and tetrafluorides, *Phys. Rev. B: Condens. Matter Mater. Phys.*, 1989, **39**(15), 11142–11145.

23 A. Miskowiec, *et al.*, Vibrational properties of uranium fluorides, *Phys. B*, 2019, **570**, 194–205.

24 E. Villa-Aleman and M. S. Wellons, Characterization of uranium tetrafluoride (UF_4) with Raman spectroscopy, *J. Raman Spectrosc.*, 2016, **47**(7), 865–870.

25 P. Gans, B. J. Hathaway and B. C. Smith, Diffuse reflectance spectra of some uranium(IV) complexes, *Spectrochim. Acta*, 1965, **21**(9), 1589–1595.

26 E. I. Khanaev, E. G. Teterin and L. A. Luk'yanova, IR spectroscopic study of dehydration products of UF_4 and PuF_4 crystal hydrates in an anhydrous HF current, *J. Appl. Spectrosc.*, 1967, **6**(6), 533–538.

27 M. A. DeVore, *et al.*, Vibrational spectroscopy of uranium tetrafluoride hydrates, *Vib. Spectrosc.*, 2021, **115**, 103277.

28 B. J. Foley, *et al.*, Probing the hydrolytic degradation of UF_4 in humid air, *Dalton Trans.*, 2022, **51**(15), 6061–6067.

29 S. N. Ghosh, W. Gordy and D. G. Hill, Paramagnetic Resonance in Uranium Salts, *Phys. Rev.*, 1954, **96**(1), 36–38.

30 A. Y. Teterin, *et al.*, Electronic structure of solid uranium tetrafluoride UF_4, *Phys. Rev. B: Condens. Matter Mater. Phys.*, 2006, **74**(4), 045101.

31 J. H. Christian, *et al.*, Characterizing the solid hydrolysis product, $UF_4(H_2O)_{2.5}$, generated from neat water reactions with UF_4 at room temperature, *Dalton Trans.*, 2021, **50**(7), 2462–2471.

32 E. Villa-Aleman, *et al.*, Raman microspectroscopy of PuO_2 particulate aggregates, *J. Nucl. Mater.*, 2019, **515**, 140–149.

33 E. Villa-Aleman, *et al.*, Raman spectroscopy: A tool to investigate alpha decay damage in a PuO_2 crystal lattice and determining sample age since calcination, *J. Raman Spectrosc.*, 2019, **50**(6), 899–901.

34 E. Villa-Aleman, *et al.*, Raman signatures from age-dating PuO_2 since last calcination, *J. Nucl. Mater.*, 2021, **551**, 152969.

35 E. Villa-Aleman, *et al.*, The electronic Raman scattering spectrum of PuO_2, *J. Raman Spectrosc.*, 2023, **54**(3), 324–332.

36 E. Villa-Aleman, *et al.*, Laser-induced annealing of aged PuO_2, *J. Raman Spectrosc.*, 2021, **52**(8), 1486–1489.

37 E. Villa-Aleman, *et al.*, Diffuse Reflectance Spectroscopy and Principal Component Analysis to Retrospectively Determine Production History of Plutonium Dioxide, *Appl. Spectrosc.*, 2022, **77**(5), 449–456.

38 J. H. Christian, *et al.*, Raman and infrared spectra of plutonium(IV) oxalate and its thermal degradation products, *J. Nucl. Mater.*, 2022, **562**, 153574.

39 J. H. Christian, *et al.*, Probing the thermal decomposition of plutonium(III) oxalate with IR and Raman spectroscopy, X-ray diffraction, and electron microscopy, *J. Nucl. Mater.*, 2023, **584**, 154596.

40 N. Vigier, *et al.*, Reaction mechanisms of the thermal conversion of Pu(IV) oxalate into plutonium oxide, *J. Alloys Compd.*, 2007, **444–445**, 594–597.

41 Y. A. Teterin, *et al.*, Electronic structure and chemical bonding in PuO_2, *Phys. Rev. B: Condens. Matter Mater. Phys.*, 2013, **87**(24), 245108.

42 A. Karelin, *et al.*, Thermal decomposition of Np(IV) and Pu (III, IV) oxalates, *J. Radioanal. Nucl. Chem.*, 1990, **143**(1), 241–252.

43 T. Vitova, *et al.*, Exploring the electronic structure and speciation of aqueous and colloidal Pu with high energy resolution XANES and computations, *Chem. Commun.*, 2018, **54**(91), 12824–12827.

44 P. S. Bagus, B. Schacherl and T. Vitova, Computational and Spectroscopic Tools for the Detection of Bond Covalency in Pu(IV) Materials, *Inorg. Chem.*, 2021, **60**(21), 16090–16102.

45 S. B. Isbill, *et al.*, Computational insights into the lattice dynamics of Pu(IV) oxalates, *J. Nucl. Mater.*, 2023, **573**, 154106.

46 J. C. Wedal, F. Furche and W. J. Evans, Density Functional Theory Analysis of the Importance of Coordination Geometry for $5f^36d^1$ versus $5f^4$ Electron Configurations in U(II) Complexes, *Inorg. Chem.*, 2021, **60**(21), 16316–16325.

47 C. J. South and L. E. Roy, Insights into the thermal decomposition of plutonium(IV) oxalate – a DFT study of the intermediate structures, *J. Nucl. Mater.*, 2021, **549**, 152864.

48 M. Pepper and B. E. Bursten, The electronic structure of actinide-containing molecules: a challenge to applied quantum chemistry, *Chem. Rev.*, 1991, **91**(5), 719–741.

49 J. C. Krupa, Optical excitations in lanthanide and actinide compounds, *J. Alloys Compd.*, 1995, **225**(1), 1–10.

50 A. C. Larson, R. B. Roof Jnr and D. T. Cromer, The crystal structure of UF_4, *Acta Crystallogr.*, 1964, **17**(5), 555–558.

51 T. K. Keenan and L. B. Asprey, Lattice constants of actinide tetrafluorides including berkelium, *Inorg. Chem.*, 1969, **8**(2), 235–238.

52 L. B. Asprey and R. G. Haire, On the actinide tetrafluoride lattice parameters, *Inorg. Nucl. Chem. Lett.*, 1973, **9**(11), 1121–1128.

53 W. H. Zachariasen, Crystal chemical studies of the 5f-series of elements. XII. New compounds representing known structure types, *Acta Crystallogr.*, 1949, **2**(6), 388–390.

54 R. Shannon, Revised effective ionic radii and systematic studies of interatomic distances in halides and chalcogenides, *Acta Crystallogr., Sect. A: Cryst. Phys., Diffr., Theor. Gen. Crystallogr.*, 1976, **32**(5), 751–767.

55 J. K. Dawson, R. W. M. D'Eye and A. E. Truswell, The hydrated tetrafluorides of uranium and plutonium, *J. Chem. Soc.*, 1954, 3922–3929.

56 J. K. Dawson, *et al.*, The preparation and some properties of plutonium fluorides, *J. Chem. Soc.*, 1954, 558–564.

57 W. H. Zachariasen, U. S. A. E. Commission and L. Argonne National, *X-ray diffraction studies of fluorides of plutonium and neptunium: chemical identity and crystal structure*, Atomic Energy Commission. MDDC, United States, 1396, Atomic Energy Commission, Oak Ridge, Tenn. 1947, 16 p.

58 Y. V. Gagarinskii, *et al.*, The crystal hydrate $UF_4{\cdot}4/3\ H_2O$, *At. Energy*, 1965, **18**(1), 43–48.

59 K. J. Pastoor, *et al.*, Structural Characterization of Uranium Tetrafluoride Hydrate ($UF_4{\cdot}2.5H_2O$), *J. Phys. Chem. C*, 2022, **126**(31), 13256–13267.

60 S. V. Borisov and G. M. Zadneprovskii, The crystal structure of $UF_4{\cdot}2.5H_2O$, *At. Energy*, 1971, **31**(1), 761–763.

61 C. J. Mandleberg and K. E. Francis, *The solubility of PuF_4 in Nitric acid solutions and the solubility product of PuF_4*, United Kingdom, 1952.

62 J. D. Moseley and R. O. Wing, *Properties of plutonium dioxide*, Rocky Flats Div., Dow Chemical Co., Denver, Colo, 1965.

63 X. Machuron-Mandard and C. Madic, Plutonium dioxide particle properties as a function of calcination temperature, *J. Alloys Compd.*, 1996, **235**(2), 216–224.

64 M. N. Myers, *Thermal decomposition of plutonium(IV) oxalate and hydrofluorination of plutonium(IV) oxalate and oxide*, General Electric Co. Hanford Atomic Products Operation, Richland, Wash, 1956.

65 P. K. Smith, *et al.*, *Effect of oxalate precipitation on PuO_2 microstructures*, United States, 1976, p. 11.

66 E. a. C. D. Y. Chudinov, *At. Energ.*, 1970, **28**, 151–153.

67 M. Goldstein, R. J. Hughes and W. D. Unsworth, Vibrational spectra of some heavy metal teftafluorides in

the solid state, *Spectrochim. Acta, Part A*, 1975, **31**(5), 621–624.

68 K. Roodenko, *et al.*, Modified phonon confinement model for Raman spectroscopy of nanostructured materials, *Phys. Rev. B: Condens. Matter Mater. Phys.*, 2010, **82**(11), 115210.

69 J. F. Corbey, *et al.*, Quantitative Microstructural Characterization of Plutonium Oxalate Auto-Degradation and Evidence for PuO_2 Nanocrystal Formation, *Eur. J. Inorg. Chem.*, 2021, **2021**(32), 3277–3291.

70 D. Hudry, *et al.*, Ultra-Small Plutonium Oxide Nanocrystals: An Innovative Material in Plutonium Science, *Chem. – Eur. J.*, 2014, **20**(33), 10431–10438.

71 F. Pointurier, C. Lelong and O. Marie, Study of the chemical changes of μm-sized particles of uranium tetrafluoride (UF_4) in environmental conditions by means of micro-Raman spectrometry, *Vib. Spectrosc.*, 2020, **110**, 103145.

72 L. M. Toth and H. A. Friedman, The IR spectrum of Pu(IV) polymer, *J. Inorg. Nucl. Chem.*, 1978, **40**(5), 807–810.

73 B. Arab-Chapelet, *et al.*, Synthesis and characterization of mixed An(IV)An(III) oxalates (An(IV)=Th, Np, U or Pu and An(III)=Pu or Am), *J. Nucl. Mater.*, 2008, **373**(1), 259–268.

74 S. A. Bryan, *et al.*, Spectroscopic monitoring of spent nuclear fuel reprocessing streams: an evaluation of spent fuel solutions via Raman, visible, and near-infrared spectroscopy, *Radiochim. Acta*, 2011, **99**(9), 563–572.

75 D. P. Armstrong, W. D. Bostick and W. H. Fletcher, An FT-IR Study of the Atmospheric Hydrolysis of Uranium Hexafluoride, *Appl. Spectrosc.*, 1991, **45**(6), 1008–1016.

76 G. L. Wagner, *et al.*, Morphologic and chemical characterization of products from hydrolysis of UF_6, *J. Fluorine Chem.*, 2015, **178**, 107–114.

77 M. C. Kirkegaard, *et al.*, Formation of a uranyl hydroxide hydrate via hydration of $[(UO_2F_2)(H_2O)]_7{\cdot}4H_2O$, *Dalton Trans.*, 2019, **48**(36), 13685–13698.

78 K. Ohwada, Uranium-fluorine lattice vibration of uranyl fluoride, *J. Inorg. Nucl. Chem.*, 1971, **33**(6), 1615–1623.

79 R. K. Thomas and H. W. Thompson, Hydrogen bonding in the vapour phase between water and hydrogen fluoride: the infrared spectrum of the 1 : 1 complex, *Proc. R. Soc. London, Ser. A*, 1997, **344**(1639), 579–592.

80 J. E. Lohr and G. Kortüm, *Reflectance Spectroscopy: Principles, Methods, Applications*, Springer Berlin Heidelberg, 2012.

81 J. C. Krupa and W. T. Carnall, Electronic structure of U^{4+}, Np^{4+}, and Pu^{4+} doped into $ThSiO_4$ single crystal, *J. Chem. Phys.*, 1993, **99**(11), 8577–8584.

82 G. K. Liu, *et al.*, Analysis of the crystal–field spectra of the actinide tetrafluorides. II. AmF_4, CmF_4, Cm^{4+}:CeF_4, and Bk^{4+}:CeF_4, *J. Chem. Phys.*, 1994, **101**(10), 8277–8289.

83 D. E. Hobart and K. Boland, Diffuse Reflectance Spectroscopy of Plutonium Solids, *Actinide Res. Quart*, 2011, **2**, 37–41.

84 J. H. Matonic, B. L. Scott and M. P. Neu, High-Yield Synthesis and Single-Crystal X-ray Structure of a Plutonium(III) Aquo Complex: $[Pu(H_2O)_9][CF_3SO_3]_3$, *Inorg. Chem.*, 2001, **40**(12), 2638–2639.

85 W. Runde, *et al.*, Synthesis and structural characterization of a molecular plutonium(IV) compound constructed from dimeric building blocks, *Chem. Commun.*, 2007, (17), 1728–1729.

86 W. Runde, *et al.*, Directed Synthesis of Crystalline Plutonium(III) and (IV) Oxalates: Accessing Redox-Controlled Separations in Acidic Solutions, *Inorg. Chem.*, 2009, **48**(13), 5967–5972.

87 S. D. Reilly, B. L. Scott and A. J. Gaunt, $[N(n\text{-}Bu)_4]_2[Pu(NO_3)_6]$ and $[N(n\text{-}Bu)_4]_2[PuCl_6]$: Starting Materials To Facilitate Nonaqueous Plutonium(IV) Chemistry, *Inorg. Chem.*, 2012, **51**(17), 9165–9167.

88 S. D. Reilly, *et al.*, Synthesis and characterization of $NpCl_4(DME)_2$ and $PuCl_4(DME)_2$ neutral transuranic An(IV) starting materials, *Dalton Trans.*, 2014, **43**(4), 1498–1501.

89 S. G. Minasian, *et al.*, Synthesis and Structure of $(Ph_4P)_2MCl_6$ (M = Ti, Zr, Hf, Th, U, Np, Pu), *Inorg. Chem.*, 2012, **51**(10), 5728–5736.

90 D. Rosario-Amorin, *et al.*, Synthesis and Coordination Chemistry of Phosphine Oxide Decorated Dibenzofuran Platforms, *Inorg. Chem.*, 2012, **51**(12), 6667–6681.

91 S. D. Reilly, *et al.*, Plutonium(IV) complexation by diglycolamide ligands—coordination chemistry insight into TODGA-based actinide separations, *Chem. Commun.*, 2012, **48**(78), 9732–9734.

92 J. H. Matonic, *et al.*, Synthesis and crystal structure of a ten-coordinate plutonium(IV) ion complexed by 2-[(diphenylphosphino)methyl]pyridine N,P-dioxide: $[Pu(NO_3)_3\{2\text{-}[(C_6H_5)_2P(O)CH_2]C_5H_4NO\}_2][Pu(NO_3)_6]_{0.5}$, *J. Chem. Soc., Dalton Trans.*, 2002, (11), 2328–2332.

93 S. I. Nikitenko and P. Moisy, Formation of Higher Chloride Complexes of Np(IV) and Pu(IV) in Water-Stable Room-Temperature Ionic Liquid $[BuMeIm][Tf_2N]$, *Inorg. Chem.*, 2006, **45**(3), 1235–1242.

94 R. F. Hess, *et al.*, Synthesis and Structural Characterization of the First Quaternary Plutonium Thiophosphates: $K_3Pu(PS_4)_2$ and $APuP_2S_7$ (A = K, Rb, Cs), *J. Am. Chem. Soc.*, 2002, **124**(7), 1327–1333.

95 Y. Zhang, E. R. Vance and T. McLeod, Diffuse reflectance spectroscopy of Np and Pu in zirconia and pyrochlore-structured $Y_2Ti_2O_7$, *J. Nucl. Mater.*, 2012, **420**(1), 278–281.

96 Y. Zhang and E. R. Vance, Diffuse reflectance spectroscopy of tetravalent neptunium and plutonium ions in ThO_2, *J. Nucl. Mater.*, 2008, **374**(1), 192–196.

97 D. J. Gregg, *et al.*, The incorporation of plutonium in lanthanum zirconate pyrochlore, *J. Nucl. Mater.*, 2013, **443**(1), 444–451.

98 Y. Zhang and E. R. Vance, Plutonium in monazite and brabantite: Diffuse reflectance spectroscopy study, *J. Nucl. Mater.*, 2008, **375**(3), 311–314.

99 TOPAS, *Bruker AXS software package Copyright 1999*. 2016.

100 S. Gates-Rector and T. Blanton, The Powder Diffraction File: a quality materials characterization database, *Powder Diffr.*, 2019, **34**(4), 352–360.